PNAS RESEARCH ARTICLE | PHYSICS OPEN ACCESS

Phase tuning of multiple Andreev reflections of Dirac fermions and the Josephson supercurrent in Al–$MoTe_2$–Al junctions

Zheyi Zhu[a], Stephan Kim[a,b], Shiming Lei[c], Leslie M. Schoop[c], R. J. Cava[c], and N. P. Ong[a,1]

Contributed by N. P. Ong; received March 13, 2022; accepted May 18, 2022; reviewed by Joseph Checkelsky and Harold Hwang

When an electron is incident on a superconductor from a metal, it is reflected as a hole in a process called Andreev reflection. If the metal N is sandwiched between two superconductors S in an SNS junction, multiple Andreev reflections (MARs) occur. We have found that, in SNS junctions with high transparency ($\tau \rightarrow 1$) based on the Dirac semimetal $MoTe_2$, the MAR features are observed with exceptional resolution. By tuning the phase difference φ between the bracketing Al superconductors, we establish that the MARs coexist with a Josephson supercurrent $I_s = I_A \sin\varphi$. As we vary the junction voltage V, the supercurrent amplitude I_A varies in step with the MAR order n, revealing a direct relation between them. Two successive Andreev reflections serve to shuttle a Cooper pair across the junction. If the pair is shuttled coherently, it contributes to I_s. The experiment measures the fraction of pairs shuttled coherently vs. V. Surprisingly, superconductivity in $MoTe_2$ does not affect the MAR features.

superconductivity | topological | Andreev reflection | Josephson | Dirac semimetal

A normal metal N sandwiched between two superconductors S forms an SNS junction. For electrons in N, the superconducting gaps in S act as steep side-walls in an unusual square-well potential. An electron in N that approaches the right N–S interface with momentum $\mathbf{p}$ is retro-reflected as a hole of momentum $-\mathbf{p}$ (Fig. 1*A*). In this Andreev reflection process (1), a Cooper pair is created in the right superconductor. When the left-moving hole reaches the left N–S interface, it again suffers a retro-reflection as an electron, while a Cooper pair is annihilated in the left S. As a result, two successive reflections shuttle one Cooper pair across the junction (green arrows). Multiple Andreev reflections (MARs) are prominently seen when a finite voltage V is applied across the junction (2). As shown in Fig. 1*A*, both excitations gain energy eV with each traversal ($e > 0$ is the elemental charge). Eventually, with n traversals (called the n^{th}-order process), the excitation acquires enough energy to surmount the potential barrier.

The investigation of topological superconductivity and pairing correlations in unconventional metals is currently a very active area of research. However, given that very few superconducting topological semimetals have been found, many experiments resort to injecting a supercurrent from a conventional superconductor to induce pairing by proximity in systems of interest. Examples include graphene (3, 4), carbon nanotubes (5), point-contact or break junctions (6, 7), Josephson ω-junctions (8), topological Bi nanowires (9), and systems exhibiting edge currents (10–12). In most of these experiments, Andreev bound states and subgap states based on Andreev reflections play central roles. Signatures specific to topological junctions arising from Andreev subgap states have been discussed by a number of groups (13–15).

Junctions with extended geometries (as opposed to break junctions) are particularly interesting, but a number of questions remain open. Can a Josephson supercurrent coexist with the MAR observed at finite V? Are the two charge-transfer phenomena mutually independent processes, or are they intimately related? Calculations have shown that an Andreev bound state strongly localized at, say, an atomic break junction can shuttle Cooper pairs as a supercurrent (16–18) (the calculations are restricted to the $V = 0$ situation). In this limit (junction spacing $d \rightarrow 0$), MARs have been observed. Here, we expand the parameter space, going to finite V in extended junctions with finite d. Aside from the emergence of MARs, the finite d implies that a sizeable fraction of the pairs are shuttled incoherently, and this dephasing feature can be studied by varying d. This regime is relevant to many of the experiments listed. Application of phase-tuning allows us to investigate the relation between MARs and the supercurrent in considerable detail.

Weak subgap, subharmonic features have long been observed in numerous experiments on (single) S–$\mathcal{I}$–S junctions (where $\mathcal{I}$ is insulator) and ascribed to various causes (19, 20). Their identification with MARs was made in ref. 2. Subsequently, microscopic calculations of MARs were compared with experiments on point-contact or break junctions (21–23). Here, we extend these pioneering experiments to a broader regime, applying the powerful

Significance

When an electron in a metal *N* is incident on the interface with a superconductor, it undergoes an Andreev reflection. A positive charge (a hole) is reflected back to *N*, while an electron pair (Cooper pair) is created in the superconductor. If *N* is sandwiched between two superconductors to form a junction, multiple Andreev reflections occur. As a result, multiple Cooper pairs are shuttled across the junction, but only a fraction of them retain phase coherence to define a supercurrent. In a Dirac semimetal, the reflections are observed with exceptional clarity. By tuning the quantum phase across the junction, we show that the supercurrent is tightly choreographed with the Andreev reflections. This allows the coherent fraction to be found.

Author affiliations: [a]Department of Physics, Princeton University, Princeton, NJ 08544; [b]Department of Electrical and Computer Engineering, Princeton University, Princeton, NJ 08544; and [c]Department of Chemistry, Princeton University, Princeton, NJ 08544

Author contributions: Z.Z. and N.P.O. designed research; Z.Z. and S.K. performed research; S.L., L.M.S., and R.J.C. contributed new reagents/analytic tools; Z.Z., S.K., S.L., and N.P.O. analyzed data; Z.Z. and N.P.O. wrote the paper; S.L. optimized crystal growth; L.M.S. supervised crystal growth; R.J.C. supervised crystal growth; and N.P.O. conceptualized experiment.

Reviewers: J.C., Massachusetts Institute of Technology; and H.H., Stanford University.

The authors declare no competing interest.

[1]To whom correspondence may be addressed. Email: npo@princeton.edu.

This article contains supporting information online at https://www.pnas.org/lookup/suppl/doi:10.1073/pnas.2204468119/-/DCSupplemental.

Published July 8, 2022.

technique of phase tuning on high-transparency SNS junctions using an asymmetric superconducting quantum interference device (SQUID) layout (6, 7, 9, 14, 24–26). Our focus is on the MARs and the Josephson effect when N is the Dirac–Weyl semimetal $MoTe_2$ [which becomes a superconductor below the critical temperature $T_c = 100$ mK (11)].

Experimental Results

Asymmetric SQUID. Flux-grown crystals of $MoTe_2$ exhibiting high residual resistivity ratios (∼1,000) and mobilities (100,000 to 150,000 cm^2/Vs) were exfoliated in air into thin flakes of nominal thickness, 100 nm, and transferred onto a SI substrate capped with a 90-nm-thick SiO_2 layer. We deposited Al wires on the surface of a flake to define four direct current (dc) SQUIDs (details in *Materials and Methods*). As shown in Fig. 1 *B*, *Inset*, the S–N–S junction, with critical current I_c, is fabricated in parallel with an auxiliary conventional S–$\mathcal{I}$–S tunnel junction with critical current I_0 (where S = Al, $n = MoTe_2$, and $\mathcal{I} = Al_2O_3$). The phases across the S–N–S and S–$\mathcal{I}$–S junctions are δ and γ, respectively. In the four devices (S1 to S4), the ratio I_0/I_c is ≥ 4. The junction width d equals 200, 300, 400, and 500 nm in devices S1, S2, S3, and S4, respectively.

When the applied current I exceeds the SQUID's critical current I_{cS}, the voltage V rises steeply. We recorded both the I–V curve and the differential resistance dV/dI vs. I measured in a magnetic field B at temperatures T from 0.035 to 1.1 K. The curves of $V(B, I)$ and $dV/dI(B, I)$ are reported as color maps in the B–I plane (the two experimentally controlled quantities).

In the regime $V = 0$ ($I < I_{cS}$), both phases δ and γ are static and related by the constraint $\delta - \gamma = \varphi$, where $\varphi \equiv 2\pi BA/\phi_0$ is the flux-induced phase shift and $\phi_0 = h/2e$ is the superconducting flux quantum (A is the loop area, and h is Planck's constant). For $V = 0$, we maximize I_{cS} under the constraint on $\delta - \gamma$ and find that the auxiliary phase γ is pinned close to $\pi/2$ if $I_0 \gg I_c$. The curve of I_{cS} vs. φ then yields the current-phase-relation (CPR) curve of the SNS junction. From the CPR, we obtain $I_0 = 93$ μA and $I_c = 29.6$ μA (*SI Appendix*, Fig. S1 and section A).

Our focus is on the finite-V regime ($I > I_{cS}$) (24). At finite V, $\delta(t)$ and $\gamma(t)$ wind rapidly at the same rate ($\dot{\delta} = \dot{\gamma}$) with their difference fixed at φ. The finite voltage across the SQUID, given by $V = \hbar\langle\dot{\gamma}\rangle/2e$ (where $\langle\cdots\rangle$ denotes time-averaged), drives a normal current I_N that flows parallel to the supercurrents I_{s0} and I_{s1} in the auxiliary and sample junctions, respectively ($I = I_{s0} + I_{s1} + I_N$).

Resistively Shunted Junction Model at Finite V. To gain insight into the MAR, it is helpful to generalize the resistively shunted junction (RSJ) model. We assume that, at finite V, the supercurrent in the S–N–S junction can be approximated by $I_{s1} \simeq I_A(V)\sin\delta$, with a V-dependent amplitude $I_A(V)$ (as $V \to 0$, $I_A(0) = I_c$). The total t-dependent current is then

$$I(V, \varphi, t) = \frac{\hbar\dot{\gamma}(t)}{2eR_\parallel} + I_0 \sin\gamma(t) + I_A(V)\sin(\gamma(t) + \varphi), \quad [1]$$

with $R_\parallel^{-1} = G = G_0 + G_1$, where G_1 is the shunt S–N–S conductance arising from the MAR and G_0 is the remaining background conductance (*SI Appendix*, section C).

We consider the two extremal cases when φ equals φ_+ (with I_{s1} parallel to I_{s0}) and φ_- (antiparallel). At $\varphi_\pm$, we have

$$I(V, \varphi_\pm, t) = \frac{\hbar\dot{\gamma}(t)}{2eR_\parallel} + [I_0 \pm I_A(V)]\sin\gamma(t), \quad [2]$$

which reduces to the equation governing the phase dynamics in a single junction (24–26). [When the geometric inductance L of the SQUID is negligible, $\varphi_+ = 0$ and $\varphi_- = \pi$. As discussed in *SI Appendix*, section D, a finite L shifts $\varphi_\pm$ from these values (26).]

We then have for the dc voltage

$$V(\varphi_\pm, I) = R_\parallel\sqrt{I^2 - I_{cS}^2(\varphi_\pm)}, \quad (I > I_{cS}(\varphi_\pm)), \quad [3]$$

with $I_{cS}(\varphi_\pm) = I_0 \pm I_A(V)$. As shown below, allowing I_A and $R_\parallel$ to acquire a V dependence yields a close description of the measured curves $V(\varphi_\pm, I)$.

Fig. 1*C* shows $V(B, I)$ (measured in S1 at 135 mK) plotted in the B–I plane. The black region ($V = 0$) is bounded by the CPR curve $I_{cS}(B)$. At fixed B, V is observed to increase steeply once I exceeds $I_{cS}(B)$, approaching a linear dependence at large V.

In Fig. 1*D* (main panel), we display a series of curves of V vs. I with B as a parameter ($B \in [-24, -2]$ μT). See *SI Appendix*, Fig. S2*A* for curves with $B \in [0, 42]$ μT. A series of steps are clearly seen in $V(B, I)$. As shown in Fig. 1 *D*, *Inset*, they persist to $V = 100$ μV. The steps appear as narrow peaks in the derivative dV/dI, which follow a subharmonic sequence $V_n = V_{max}/n$. In Fig. 1*E*, we show that as T is raised to 1.1 K, the peaks converge to zero.

MARs under Phase Tuning. A key feature emerges when we investigate the effect of phase tuning on the sequence of peaks. To see this, we plot the color map of $dV/dI(B, I)$ in the B–I plane (Fig. 2*A*). Above the CPR curve $I_{cS}(B)$, we see a sheaf of sharply defined sinusoidal curves (light-blue wavy curves) that appear to peel off from the CPR curve. As we approach the CPR curve from above ($V \to 0^+$ in the limit $n \gg 1$), the sinusoidal curves smoothly approach the functional form of the CPR curve. (As shown below, this smooth evolution vanishes abruptly when T is lowered below $T_c = 100$ mK.) Since B is linear in the phase φ, we infer that the sinusoidal curves are tracking a component of I that varies sinusoidally with φ. This φ dependence is the hallmark of a Josephson supercurrent.

We next show that each sinusoidal curve also corresponds to an abrupt change in the MAR order ($n \to n - 1$) at a voltage V_n that is independent of φ. Using the I–V curves in Fig. 1*D*, we transform the vertical axis from I to V. Under this transformation (Fig. 2), each sinusoidal curve in S1 collapses to a flat line. The voltage V_n on each line fits the subharmonic sequence $V_n = V_{max}/n$ for $n = 2, 3, 4\cdots$ (*SI Appendix*, Fig. S2*C*). The parameter V_{max} has the T-independent value 200 μV below 300 mK, but decreases as $T \to T_c^{Al}$ (1.2 K), consistent with $V_{max} = 2\Delta/e$, where Δ is the energy gap of Al (*SI Appendix*, Fig. S2*B*). These are key signatures of MARs (2, 21–23).

Increasing the junction spacing d strongly damps both the critical current I_c and the amplitude of the sinusoidal curves. In Fig. 3, we show color maps of $dV/dI(B, I)$ for the four devices S1$\cdots$ S4 measured at 340 mK. Although, at 340 mK, I_c (defined as half the peak-to-trough excursion) decreases steeply with d (*SI Appendix*, Fig. S2*D*), the supercurrent is observable well beyond $d = 500$ nm at 135 mK. Hereafter, we focus on results from S1.

Quantifying Normal Current and Supercurrent.

MAR-induced steps in I–V curve. The striking staircase profile of $V(\varphi, I)$ (Fig. 1*D*) provides a vital clue to the MAR charge transfer. When V lies in the interval $V_n \leq V < V_{n-1}$, where $V_n = 2\Delta/ne$, the n^{th}-order process is dominant because of the divergent density of states (DOS) at the gap edge in Al. In an

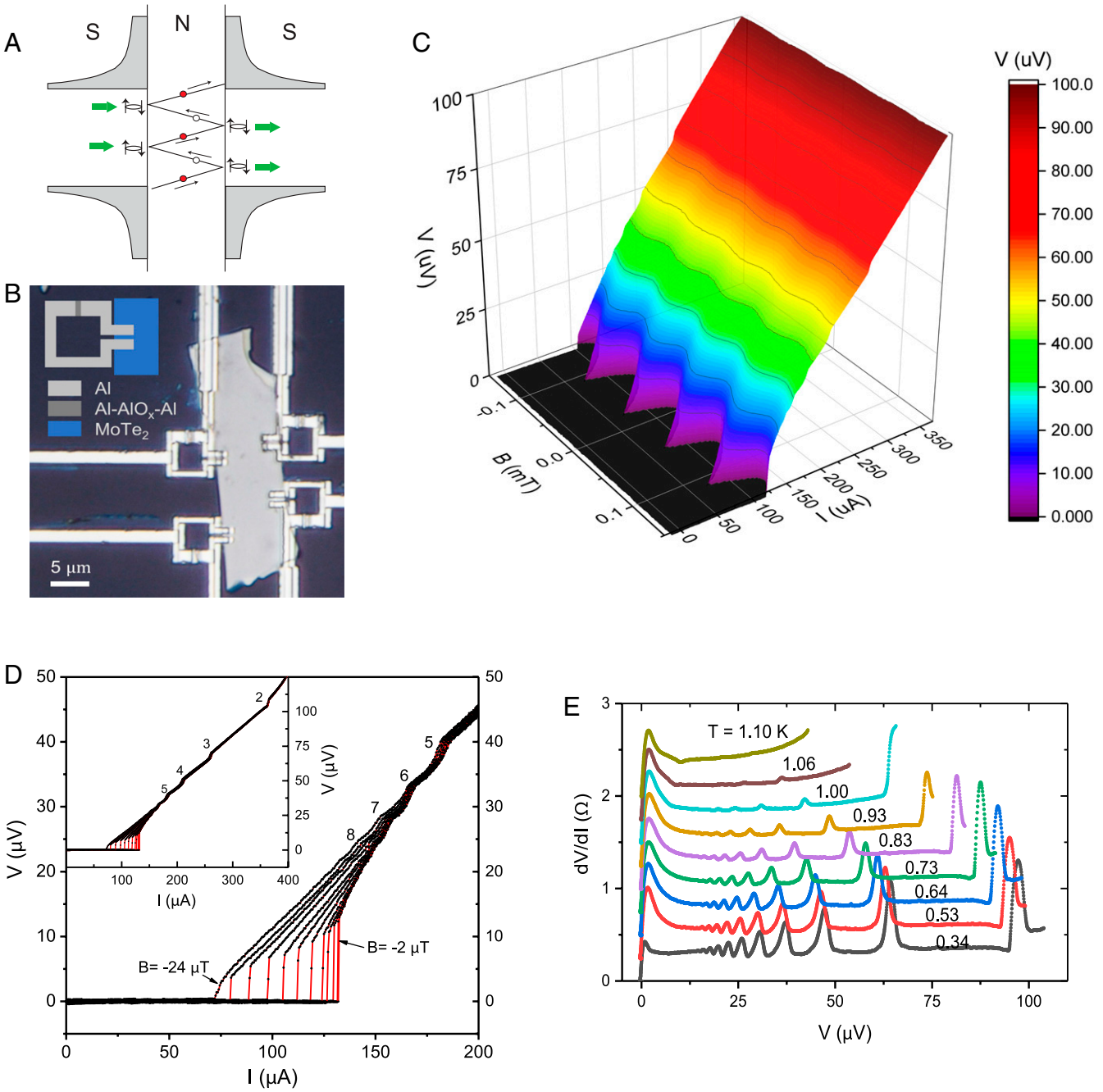

Fig. 1. MAR in the asymmetric SQUID layout with the *S–N–S* junction based on $MoTe_2$. *A* shows a sketch of the 5^{th}-order MAR process. Right-moving electrons (red circles) are Andreev-reflected as left-moving holes (white circles). After five traversals, the excitation gains sufficient energy to scale the gap barrier. In the process, two pairs (green arrows) are shuttled across. The DOS in Al are shaded gray. *B* shows four devices fabricated on an exfoliated crystal of $MoTe_2$ (gray area). The sketch in *B*, *Inset* shows the *S–N–S* (*S–I–S*) junction on the right (top) branch. The applied flux $\phi_a = BA$ pierces the enclosed rectangle. In *C*, the color map comprises 150 *I–V* curves with spacing $\Delta B = 2$ μT (color scale in vertical bar) measured in S1 at $T = 135$ mK. At fixed *B*, *V* increases steeply once *I* exceeds the SQUID critical current $I_{cS}(B)$ (the CPR curve). If *V* is held fixed, the current varies periodically with vs. *B* up to $V \sim 80$ μV [thin black curves are contours of $V(B, I)$]. *D* (main panel) shows the *I–V* curves with *B* varying from −24 μT to −2 μT in steps of 2 μT. Subharmonic steps (*n* as indicated) are visible up to $V = 105$ μV (*D*, *Inset*). Peaks in *dV/dI* at the steps occur at $V_n = V_{max}/n$ ($n = 2, 3, \cdots$). *D* shows traces of *dV/dI* vs. *V* for $0.34 < T < 1.10$ K. As $T \to T_c^{Al}$, $V_{max} \to 0$ in accord with MAR.

ideal junction (transparency $\tau = 1$), the number of pairs shuttled is $n/2$ or $(n-1)/2$ for n even or odd, respectively (for n odd, a quasiparticle is also transferred). In both cases, the total charge shuttled is ne. We have n channels when $V_n \leq V < V_{n-1}$. At either end of the interval, the channel number abruptly changes by one.

Since $k_B T \ll \Delta$ at 135 mK, the normal current $I_{N1}^{(n)}$ in the shunt conductance, $G_1^{(n)}$, derives overwhelmingly from pairs that are shuttled incoherently by MARs. As we show below (Fig. 4*A*), the shuttled pairs give rise to both a normal current $I_{N1}^{(n)} = VG_1^{(n)}$ and a supercurrent; the former responds only to V whereas the latter is sensitive to φ.

From the staircase profile, we infer a simple expression for $G_1^{(n)}$. For transparency $\tau = 1$, the abrupt change in conductance at $V = V_n$, $\Delta G_1 = G_1^{(n+1)} - G_1^{(n)}$, equals a constant g (the conductance for one traversal). This implies $G_1^{(n)} = ng$.

In a nonideal junction with $\tau < 1$, classical scattering reduces the transmission probability by the amount $(1-\tau)$ at each reflection. Instead of $G_1^{(n)} = ng$, we have

$$G_1^{(n)} = g(1+\tau+\cdots+\tau^{n-1}) = g(1-\tau^n)/(1-\tau). \quad [4]$$

As shown below, Eq. **4** leads to a quantitative description of $V(\varphi_\pm, I)$.

Shuttled pair current. We turn next to the Josephson supercurrents in the auxiliary and sample junctions, I_{s0} and I_{s1}, respectively. The n^{th}-order sinusoidal curve in the dV/dI map traces the variation of I vs. φ with $V = V_n$ (hereafter, we use φ in place of B). The maximum and minimum values attained by the current are called I_{n+} and I_{n-}, respectively. They occur at the extremal phases φ_+ and φ_-, respectively.

By Eqs. **2** and **3**, we have $I_{n\pm}^2 = (V_n/R_\parallel)^2 + [I_0 \pm I_A]^2$. Thus, the observed values $I_{n\pm}$ yield the observed amplitudes $I_A^{(n)}$, viz.

$$I_{A,obs}^{(n)} = [I_{n+}^2 - I_{n-}^2]/(4I_0). \quad [5]$$

These are plotted as black circles in Fig. 4*A*. Initially, $I_{A,obs}^{(n)}$ increases linearly with n, but deviates downward when n exceeds six (Fig. 4 *A*, *Inset*). To us, the initial n-linear growth of $I_{A,obs}^{(n)}$ is persuasive evidence that the supercurrent derives from the population of Cooper pairs that are shuttled coherently.

At large n ($V \to 0$), we expect $I_{A,obs}^{(n)}$ to saturate since it cannot exceed the critical current I_c at $V = 0$. We propose that saturation occurs because of the slight attenuation of the probability current at each reflection, analogous to Eq. **4**. Thus, $I_A^{(n)} \sim 1+\tau+\cdots+\tau^{n-1}$, which we write as

$$I_A^{(n)} = I_c[1-\tau^{n-1}]. \quad [6]$$

Using Eq. **6** to fit the data in Fig. 4*A*, we find that $I_c = 27$ μA, close to $I_c = 29.6$ μA obtained in the CPR. The agreement supports the reasoning behind Eq. **6**. The value of τ is found to be 0.924, slightly smaller than $\tau = 0.95$ from the CPR fit values in *SI Appendix*, Eq. **S3**.

In Fig. 4*A*, we also plot (as blue squares) the normal current in the sample junction $I_{N1}^{(n)}$, the product of V_n and $G_1^{(n)}$ (for g, we use the value from the fit in Eq. **7**). Despite the step-wise increase in G_1 with n, the decrease of $V \sim 1/n$ forces $I_{N1}^{(n)}$ to decrease monotonically. By contrast, $I_A^{(n)}$ (red and black symbols) increases monotonically before saturating at I_c. Both currents reflect the series $1+\tau+\cdots+\tau^n$.

The saturation $I_A \to I_c$ in the limit $V \to 0$ implies that the coherent fraction of shuttled Cooper pairs accounts for the entire Josephson supercurrent observed in the dissipationless state. This agrees with the smooth evolution of the sinusoidal curves to merge continuously with the CPR curve in the limit $n \gg 1$ observed in Fig. 2.

Heuristically, using Eqs. **4** and **6**, we can adopt the generalized RSJ model to describe the measured curves $V(\varphi_\pm, I)$ by the expressions

$$V(\varphi_\pm, I) = \frac{\sqrt{I^2 - [I_0 \pm I_A^{(n)}]^2}}{G_0 + G_1^{(n)}}, \quad [7]$$

where $n = \mathrm{Int}[V_{max}/V]$. The fits are shown as red curves in Fig. 4*B*. A more sensitive test of the fits is to compare them against the total observed conductances $G_{obs}(\varphi_\pm, I) \equiv [I^2 - (I_0 \pm I_A^{(n)})^2]^{\frac{1}{2}}\, V(\varphi_\pm, I)^{-1}$ (Fig. 4 *B*, *Inset*). As seen, both curves of $G_{obs}(\varphi_\pm, I)$ fit well to Eq. **7**. From the fits, we find for φ_- (and φ_+),

$$\tau = 0.93\ (0.92), \quad G_0 = 3.00\ (2.94)\ \mathrm{S}, \quad g = 0.32\ (0.20)\ \mathrm{S}. \quad [8]$$

The value of τ is in agreement with the fit to Eq. **6**. (For φ_+, a discontinuous jump of V occurs at the threshhold current I_{cS}. This implies a finite inertial term in the phase dynamics represented by a shunt capacitor C, which is neglected for simplicity.)

Discussion and Outlook

Andreev Reflections Below T_c of $MoTe_2$. We note that the pairing "glue" of the shuttled pairs originates from Al. In $MoTe_2$, the onset of superconductivity below $T_c = 100$ mK allows us to see how the Josephson supercurrent associated with the shuttled pairs is changed by the intrinsic pairing field $\hat{\psi}$. Our initial expectation was that $\hat{\psi}$ should strongly enhance the Josephson amplitude I_A. To our surprise, however, it has no observable effect. Fig. 4*C* and *SI Appendix*, Fig. S3 show the superposition of color maps measured at 135 mK and 35 mK (the former is Fig. 2*A*). As discussed above, at 135 mK, the sinusoidal curves associated with MARs evolve smoothly as a sheaf of curves peeling away from the CPR curve I_c vs. B. By contrast, at 35 mK, the dissipationless region (dark yellow) covers a larger area, reflecting the sharp increase in the critical current I_c. Interestingly, the MAR-induced sinusoidal curves remain unchanged from the ones at 135 mK. In the superposition, we have plotted the MAR curves observed at 35 mK in blue (they are unobservable in the dark yellow region bounded by the CPR curve $I_c(B)$). The corresponding curves at 135 mK are plotted in yellow. It may be seen that each sinusoidal curve measured at 35 mK is continuous with the curve at 135 mK across the CPR curve $I_c(B)$. The emergence of bulk superconductivity in $MoTe_2$ leaves the MAR curves unaffected.

To analyze this observation, we note that the MAR process shuttles Cooper pairs from one Al contact to the other. The pairing correlations of the shuttled pairs originate from the conventional phonon-mediated mechanism in Al. Fig. 4*C* shows that the emergence of pairing in bulk $MoTe_2$ neither strengthens nor weakens the coherence of the shuttled pairs. The long-range shuttling mechanism persists independent of any additional pairing attraction induced by $\hat{\psi}$. An interesting possibility is that the symmetry induced by s-wave pairing in Al is incompatible with, and orthogonal to, the intrinsic pairing of the Dirac electrons in the bulk.

In experiments to be reported elsewhere, we find that the intrinsic Ginzburg–Landau order parameter $\hat{\Psi}$ (characterizing the superconducting state of $MoTe_2$) exhibits weak phase rigidity. At 20 mK, the switch to dissipative behavior as B increases actually reflects the melting of the vortex solid to the vortex liquid state, triggered by the loss of phase rigidity (rather than disappearance of the pair condensate). Because the modulus of the order parameter $|\hat{\Psi}|$ remains finite in the vortex liquid, we should expect the coherence of the pairs shuttled by MAR to be enhanced especially close to the CPR curve, but this is not observed. The unchanged MAR sinusoidal curves in Fig. 4*C* suggest that the conventional s-wave pairing in the shuttled pairs is orthogonal to the intrinsic pairing mechanism in $MoTe_2$. This result will be explored further in future experiments.

High Transparency. The high transparency observed in our *SNS* junctions is remarkable, given the large mismatch of the Fermi

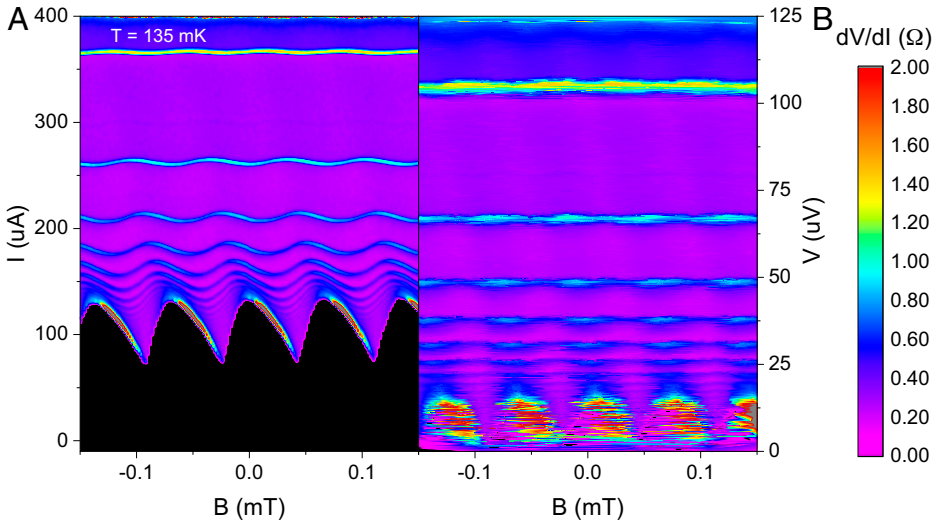

Fig. 2. Color maps of the differential resistance $dV/dI(B, I)$ measured in S1 at 135 mK, displayed in the (B, I) plane (*A*) and the (B, V) plane (*B*), with scale bar on the right. In *A*, the black area ($dV/dI = 0$) is bounded by the CPR curve $I_{cS}(B)$. Above the CPR, the series of sinusoidal curves trace the variation of narrow peaks in dV/dI vs. *B*. In *B*, the vertical axis is transformed to *V* using the *I*–*V* curve at each *B*. Each sinusoidal curve collapses to a flat line with *V* fixed at the MAR voltage $V_n = V_{max}/n$.

momenta between Al and $MoTe_2$. In conventional systems such a large mismatch leads to severe degradation of the transparency. For Dirac/Weyl fermions, we argue that strong suppression of backscattering is responsible for the large τ. The earliest example was proposed by Ando et al. (27) to explain the high conductance of carbon nanotubes. In the two-spinor state $\psi(\mathbf{k}) = (F_A, F_B)^{\mathrm{T}}$ of momentum $\mathbf{k}$ on the honeycomb lattice, the relative phase ϕ between the amplitudes F_A and F_B for occupying the A vs. B sublattice sites is given by $\tan\phi = k_y/k_x$. The angle ϕ is also the orientation of the pseudospin $\boldsymbol{\sigma}$. Most scattering potentials are too weak to change $\boldsymbol{\sigma}$, so it is conserved in each scattering event. This leads to suppression of backscattering events $\mathbf{k} \to -\mathbf{k}$, which flip $\boldsymbol{\sigma}$. In $MoTe_2$, the backscattering suppression is closer to the situation in topological insulators (28) and Weyl semimetals (29).

Now, the physical spin $\mathbf{s}$ (rather than $\boldsymbol{\sigma}$) is conserved at each scattering event from a nonmagnetic impurity. Because of spin-momentum locking and distinct spin textures around the Fermi surface, conservation of $\mathbf{s}$ again leads to strong suppression of backscattering. Lastly, the well-known Klein paradox, which leads to zero classical reflection at a step potential in graphene (30, 31), also originates from conservation of $\boldsymbol{\sigma}$. However, Klein tunneling requires Dirac states on both sides of the interface, which is not the case here. (If a thin layer of proximitized $MoTe_2$ were to be present between N and S, the Klein paradox scenario could apply. We rule this out because the gap measured by MAR is the full gap in Al, rather than the much smaller proximity gap.) For these reasons, we argue that the backscattering suppression by conservation of $\mathbf{s}$ is the most likely reason for the large transparency. Future work will

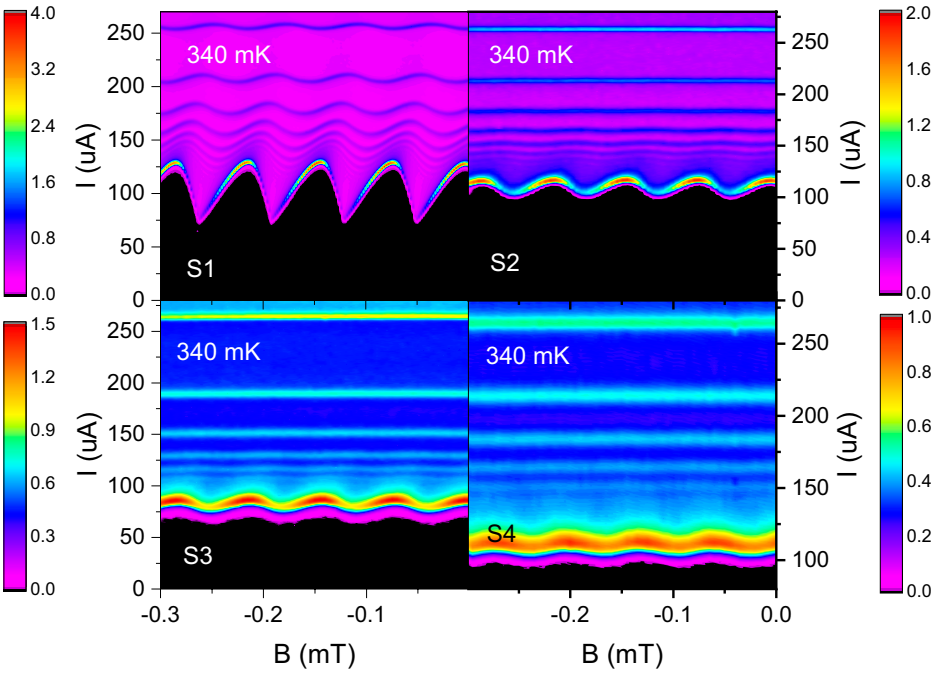

Fig. 3. Comparison of color maps of $dV/dI(I, B)$ measured in devices S1 to S4 at $T = 340$ mK. The junction spacing *d* is 200, 300, 400, and 500 nm in S1 to S4, respectively. As *d* increases, the supercurrent amplitude I_c inferred from the CPR decreases rapidly at 340 mK (*SI Appendix*, Fig. S2*D*). Unlike at 135 mK, dV/dI is not strictly zero below the CPR curve because of thermally excited quasiparticles.

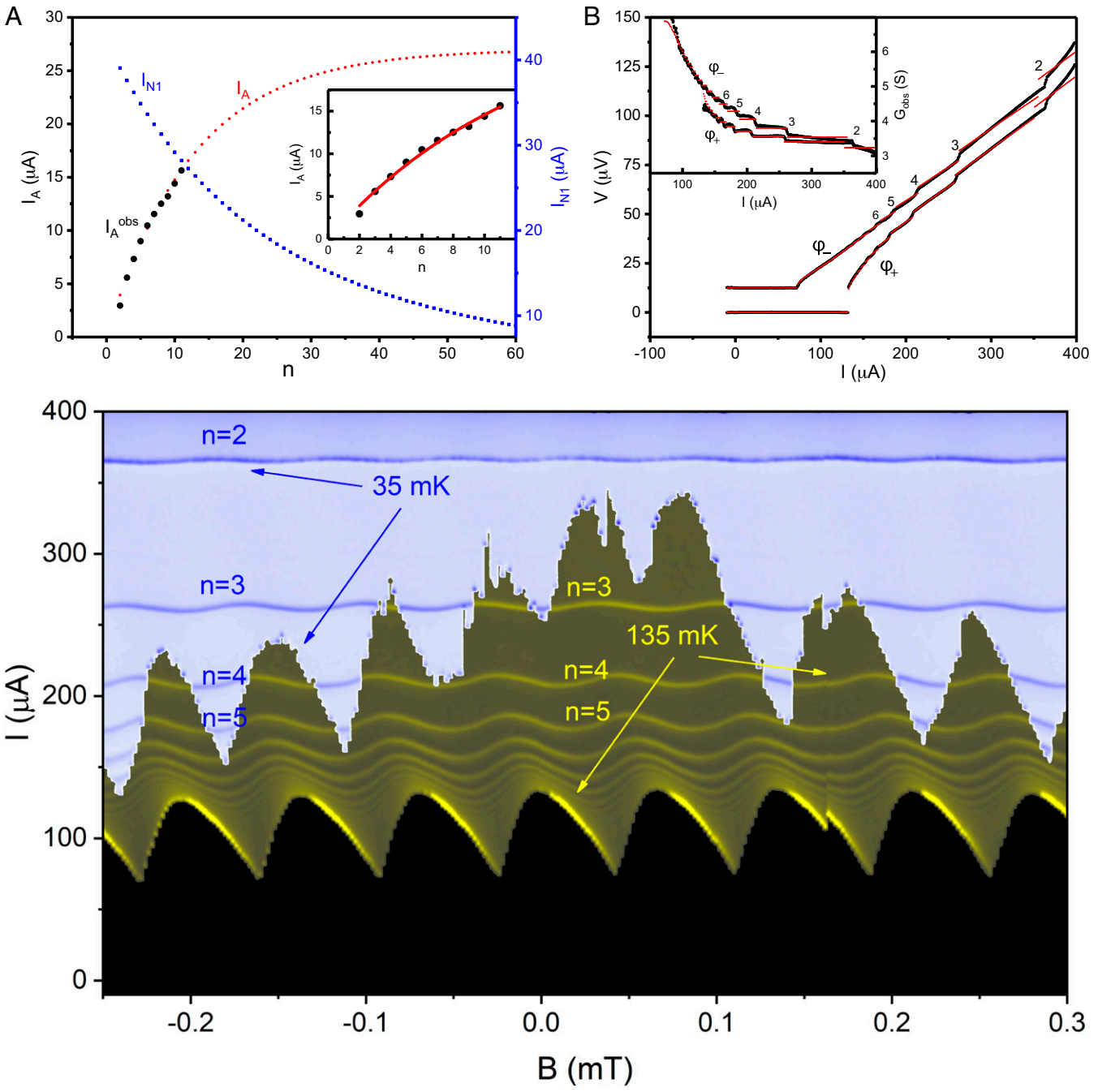

Fig. 4. Fits to the supercurrent amplitude $I_{A,obs}^{(n)}$, the *I–V* curves, and total conductance G_{obs} in device S1. (*A*) The observed supercurrent amplitude $I_{A,obs}^{(n)}$ vs. n (Eq. **5**, black circles) compared with $I_A^{(n)}$ calculated using Eq. **6** (red circles). The best fit is obtained with $I_c = 27$ μA and $\tau = 0.924$. The normal current $I_{N1}^{(n)} = V_n G_1^{(n)}$ is plotted as blue squares. The data for $I_{A,obs}^{(n)}$ and fit are shown in expanded view in *A*, *Inset*. In *B* (main panel), we compare the measured $V(\varphi_\pm, I)$ (black curves) with the best fit to Eq. **7** (red curves). The integer n at each step is indicated. For clarity, the curve $V(\varphi_+, I)$ is shifted upwards by 12.5 μA. *B*, *Inset* shows the same fits compared against the observed conductances $G_{obs}(\varphi_\pm, I)$ defined below Eq. **7**, which provide a more sensitive test for the fits. *C* is the superposition of the color maps of $dV/dI(I, B)$ measured at 135 mK and 35 mK. The MAR sinusoidal curves at 135 and 35 mK are shown in yellow and blue, respectively. The dissipationless regions at 135 mK and 35 mK are shaded in black and dark yellow, respectively. The superposition demonstrates that the MAR curves are identical at the two temperatures within our resolution. The increase in I_c below T_c (100 mK) does not affect the magnitude or positions of the MAR curves. *SI Appendix*, Fig. S3 displays the two color maps in separate panels.

test if Dirac/Weyl semimetals invariably lead to high-transparency *SNS* junctions.

A related question is whether new regimes can be accessed in the two-dimensional (2D) limit using monolayers of $MoTe_2$ (or other van der Waals semimetals). The phase-tuning approach applied to investigate possible 2D superconductivity is promising. However, we have found that technical problems related to sandwiching monolayer $MoTe_2$ between BN films are formidable.

In summary, utilizing the asymmetric SQUID technique to tune φ across extended *SNS* junctions, we have found that MARs executed by the Dirac electrons in $MoTe_2$ are observed with exceptional resolution in the $I-V$ curves. Depending on V, orders as high as $n = 12$ are resolved. The modulation of the MAR features vs. φ provides direct evidence that a Josephson supercurrent coexists with the MAR. By measuring how the amplitude I_A varies with V, we find that the supercurrent

is intimately related to the MAR. At large V (small n), the well-resolved steps in V correspond to a step decrease in the number of conductance channels for the pairs that are shuttled incoherently. Even at $n = 2$, the coherently shuttled pairs in device S1 produce a supercurrent that is detectable (Fig. 2*A*). In the opposite limit $V \to 0$, nearly all pairs are shuttled coherently. As a result, the amplitude I_A saturates to I_c obtained in the CPR (Fig. 4*A*). While the MAR process is the cause of the striking staircase pattern vividly apparent in the color maps in Figs. 2 and 3, the experiment demonstrates that, in extended junctions, the bulk of the normal current and the coexisting supercurrent actually arise from the pairs that are shuttled incoherently and coherently, respectively, in the wake of the lone injected electron. Within our resolution, the shuttled pairs account for essentially the entire Josephson supercurrent measured when $V = 0$ (above T_c of $MoTe_2$).

The ability to measure how the amplitude I_A and other parameters (n, τ, g, $\cdots$) vary with V in phase-tuned junctions may lead to a more quantitative treatment of pairing correlations in the finite-V regime, especially in unconventional platforms (13–15). Understanding the conditions under which an intrinsic pairing field can affect the supercurrent conveyed by the shuttled pairs will provide a novel way to probe an unconventional superconductor.

Materials and Methods

A. Current Definitions. We provide a glossary of the current parameters and definitions.

I is the total current applied to the SQUID.
I_{cS} is the critical current of the SQUID.
I_0 is the critical current of the auxiliary junction.
I_c is the critical current of the sample junction when $V = 0$.
$I_A(V)$ is the V-dependent amplitude of the Josephson supercurrent at finite V.
I_1 is the prefactor of the sample junction in *SI Appendix*, Eq. **S1**.
$I_{n\pm}$ are the maximum and minimum values of I in the sinusoidal curve with $V = V_n$.
I_{N1} and I_{N0} are the normal currents in the sample and auxiliary junctions, respectively, at finite V.
I_N is the total normal current in the SQUID.
I_{s0} is the supercurrent in the auxiliary junction.
I_{s1} is the supercurrent in the sample junction.

B. Device Fabrication and Measurement. We used double-layer e-beam lithography, in combination with tilted-substrate thermal evaporation, to fabricate the S–$\mathcal{I}$–S junction. Initially, the substrate is spin-coated with methyl methacrylate (MMA) EL11 at 3,000 rpm for 30 s twice and baked at 175 °C for 5 min, followed by spin-coating with poly(methyl methacrylate) (PMMA) 950 A07 at 4,000 rpm for 60 s and then baked at 175 °C for 5 min. Next, the SQUID pattern was e-beam written by using the Raith eLiNE writer with beam energy set at 30 kV, aperture at 10 μm, and the dose level at ∼300 μC/cm^2. After developing in methyl isobutyl ketone (MIBK) solution (MIBK:isopropanol [IPA] = 1:3) for 3 min and rinsing in IPA solution for 1 min, we fabricated a suspended bridge, using a half-dose beam to remove the underlying MMA layer, while keeping the suspended upper PMMA layer intact. The chip with the pattern defined was placed inside a thermal evaporator equipped with a tiltable stage, with vacuum at $\sim 5 \times 10^{-7}$ mbar. To remove residual resist and several (oxidized) monolayers of $MoTe_2$, we exposed the chip to a radiofrequency argon plasma in situ. After cleansing, the first layer of Al (60 nm) was deposited at a rate of 10 Å/s. Then, a mixture of Ar/O_2 (10% O_2) was injected into the chamber for 30 min at 5×10^{-3} mbar to oxidize the Al. A second layer of Al (120 nm) was next deposited with the angle set at a new value to define an overlapping Al–AlO_x–Al junction under the suspended PMMA resist bridge. Finally, the device was immersed in acetone to wash off the extra Al layer.

The I–V measurements were performed in a top-loading wet dilution refrigerator (Oxford Instruments Kelvinox TLM400) with base temperature of 15 to 20 mK. The dc bias and alternating-current excitation current was provided by an Agilent 33220A function generator with a bias resistance of 100 kΩ. After preamplification (NF LI-75A preamplifier), the SQUID voltage V was fed to a lock-in amplifier (Stanford Research SR830) for dV/dI measurement, as well as a nanovoltmeter (Keithley 2182A) for I–V measurement. Data above 300 mK were acquired in a Heliox Helium-3 cryostat with base temperature of 340 mK.

Data Availability. Data to recreate curves in figures have been deposited in the Harvard Dataverse (https://doi.org/10.7910/DVN/NAMOHV) (32). All study data are included in the article and/or supporting information.

ACKNOWLEDGMENTS. We are grateful to Wudi Wang for providing invaluable assistance. We thank the reviewers for helpful and insightful comments. The research was supported by US Department of Energy Award DE-SC0017863 (to N.P.O.) and the US NSF Materials Research Science and Engineering Centers Award DMR-2011750 (to N.P.O., L.M.S., and R.J.C.). We also acknowledge the support of Gordon and Betty Moore Foundation's Emergent Phenomena in Quantum Systems initiative through Grants GBMF9466 (to N.P.O.) and GBMF9064 (to L.M.S.).

1. A. F. Andreev, The thermal conductivity of the intermediate state in superconductors. *Zh. Eksp. Teor. Fiz.* **46**, 1823 (1964). [*Sov. Phys. JETP* **19**, 1228 (1964)].
2. T. M. Klapwijk, G. E. Blonder, M. Tinkham, Explanation of subharmonic energy gap structure in superconducting contacts. *Physica* **109-110B**, 1657–1664 (1982).
3. H. B. Heersche, P. Jarillo-Herrero, J. B. Oostinga, L. M. K. Vandersypen, A. F. Morpurgo, Bipolar supercurrent in graphene. *Nature* **446**, 56–59 (2007).
4. X. Du, I. Skachko, E. Y. Andrei, Josephson current and multiple Andreev reflections in graphene SNS junctions. *Phys. Rev. B Condens. Matter Mater. Phys.* **77**, 184507 (2008).
5. J.-D. Pillet *et al.*, Andreev bound states in supercurrent-carrying carbon nanotubes revealed. *Nat. Phys.* **6**, 965–969 (2010).
6. M. Zgirski *et al.*, Evidence for long-lived quasiparticles trapped in superconducting point contacts. *Phys. Rev. Lett.* **106**, 257003 (2011).
7. L. Bretheau, C. O. Girit, C. Urbina, D. Esteve, H. Pothier, Supercurrent spectroscopy of Andreev states. *Phys. Rev. X* **3**, 041034 (2013).
8. E. Strambini *et al.*, The ω-SQUIPT as a tool to phase-engineer Josephson topological materials. *Nat. Nanotechnol.* **11**, 1055–1059 (2016).
9. A. Murani *et al.*, Ballistic edge states in Bismuth nanowires revealed by SQUID interferometry. *Nat. Commun.* **8**, 15941 (2017).
10. S. Hart *et al.*, Induced superconductivity in the quantum spin Hall edge. *Nat. Phys.* **10**, 638–643 (2014).
11. W. Wang *et al.*, Evidence for an edge supercurrent in the Weyl superconductor $MoTe_2$. *Science* **368**, 534–537 (2020).
12. Y. Wang *et al.*, Proximity-induced spin-triplet superconductivity and edge supercurrent in the topological Kagome metal, $K_{1-x}V_3Sb_5$, cond-mat. *arXiv* [Preprint] (2020). https://arxiv.org/abs/2012.05898 (18 December 2020).
13. P. San-Jose, J. Cayao, E. Prada, R. Aguado, Multiple Andreev reflection and critical current in topological superconducting nanowire junctions. *New J. Phys.* **15**, 075019 (2013).
14. Y. Peng, F. Pientka, E. Berg, Y. Oreg, F. von Oppen, Signatures of topological Josephson junctions. *Phys. Rev. B* **94**, 085409 (2016).
15. F. Pientka *et al.*, Topological superconductivity in a planar Josephson junction. *Phys. Rev. X* **7**, 021032 (2017).
16. A. Furusaki, H. Takayanagi, M. Tsukada, Theory of quantum conduction of supercurrent through a constriction. *Phys. Rev. Lett.* **67**, 132–135 (1991).
17. C. W. J. Beenakker, H. van Houten, Josephson current through a superconducting quantum point contact shorter than the coherence length. *Phys. Rev. Lett.* **66**, 3056–3059 (1991).
18. A. Furusaki, Josephson current carried by Andreev levels in superconducting quantum point contacts. *Superlattices Microstruct.* **25**, 809–818 (1999).
19. B. N. Taylor, E. Burnstein, Excess currents in electron tunneling between superconductors. *Phys. Rev. Lett.* **10**, 14 (1963).
20. S. M. Marcus, The magnetic field dependence of the $2\Delta/n$ structure observed in Pb-PbO-Pb superconducting tunneling junctions. *Phys. Lett.* **19**, 623 (1966).
21. D. Averin, A. Bardas, ac Josephson effect in a single quantum channel. *Phys. Rev. Lett.* **75**, 1831–1834 (1995).
22. E. N. Bratus', V. S. Shumeiko, G. Wendin, Theory of subharmonic gap structure in superconducting mesoscopic tunnel contacts. *Phys. Rev. Lett.* **74**, 2110–2113 (1995).
23. J. C. Cuevas, A. Martín-Rodero, A. L. Yeyati, Hamiltonian approach to the transport properties of superconducting quantum point contacts. *Phys. Rev. B Condens. Matter* **54**, 7366–7379 (1996).
24. A. Th. A. M. De Waele, R. De Bruyn Ouboter, Quantum interference phenomena in point contacts between two superconductors. *Physica* **41**, 225–254 (1969).
25. T. A. Fulton, L. N. Dunkleberger, R. C. Dynes, Quantum interference properties of double Josephson Junctions. *Phys. Rev. B* **6**, 855 (1972).
26. A. Barone, G. Paterno, *Applications and Physics of the Josephson Effect* (John Wiley and Sons, Hoboken, NJ, 1982).
27. T. Ando, T. Nakanishi, R. Saito, Berry's phase and absence of back scattering in carbon nanotubes. *J. Phys. Soc. Jpn.* **67**, 2857–2862 (1998).
28. L. Fu, C. L. Kane, Topological insulators with inversion symmetry. *Phys. Rev. B Condens. Matter Mater. Phys.* **76**, 045302 (2007).
29. S. Uchida, T. Habe, Y. Asano, Andreev reflection in Weyl semimetals. *J. Phys. Soc. Jpn.* **83**, 064711 (2014).
30. C. W. J. Beenakker, Specular Andreev reflection in graphene. *Phys. Rev. Lett.* **97**, 067007 (2006).
31. M. I. Katsnelson, K. S. Novoselov, A. K. Geim, Chiral tunneling and the Klein paradox in graphene. *Nat. Phys.* **2**, 620–625 (2006).
32. Z. Zhu et al., Phase tuning of multiple Andreev reflections of Dirac fermions and the Josephson supercurrent in Al-Mo Te2-Al junctions. Harvard Dataverse. https://doi.org/10.7910/DVN/NAMOHV. Deposited 16 May 2022.